Observation of Floquet topological phases with large Chern numbers

Kai Yang,[1,2,3,*] Shaoyi Xu,[1,2,3,*] Longwen Zhou,[4,*,†] Zhiyuan Zhao,[1,2,3] Tianyu Xie,[1,2,3] Zhe Ding,[1,2,3] Wenchao Ma,[5] Jiangbin Gong,[6,7] Fazhan Shi,[1,2,3] and Jiangfeng Du[1,2,3,‡]

[1]*CAS Key Laboratory of Microscale Magnetic Resonance and School of Physical Sciences, University of Science and Technology of China, Hefei 230026, China*

[2]*CAS Center for Excellence in Quantum Information and Quantum Physics, University of Science and Technology of China, Hefei 230026, China*

[3]*Hefei National Laboratory, University of Science and Technology of China, Hefei 230088, China*

[4]*College of Physics and Optoelectronic Engineering, Ocean University of China, Qingdao 266100, China*

[5]*Department of Chemistry, Massachusetts Institute of Technology, Cambridge, Massachusetts 02139, USA*

[6]*Department of Physics, National University of Singapore, Singapore 117551*

[7]*Centre for Quantum Technologies, National University of Singapore, Singapore 117543*

(Received 5 September 2022; accepted 8 November 2022; published 21 November 2022)

Floquet engineering offers a powerful approach to the generation of nonequilibrium topological phases with large topological invariants and hence a proliferation of topological edge modes. It is thus of importance to develop feasible experimental approaches to detect such topological phases. Using the nitrogen-vacancy center in diamond and its synthetic dimensions, here we experimentally demonstrate how Floquet Chern insulator phases can be clearly detected through imaging the static and dynamic spin textures in momentum space. In particular, we simulate a periodically quenched generalized Haldane model and observe different topological phases with Chern numbers $C = 1, 2, 4$. In addition to confirming the versatility of Floquet driving in generating phases with large Chern numbers, this work clearly establishes an experimental method to detect Floquet topological phases in two and higher spatial dimensions.

DOI: 10.1103/PhysRevB.106.184106

I. INTRODUCTION

Floquet systems can host rich nonequilibrium topological phases induced by time-periodic driving fields [1–4]. They feature large topological numbers [5–8], unique symmetry classifications [9–11], and anomalous edge states with no static analog [12–14]. The experimental observation of Floquet topological matter in cold atoms [15–17], photonic setups [18–20], solid state systems [21–23], etc., further stimulated considerable research activities to realize, engineer, control, and detect quantum materials from a dynamical perspective [24].

Given that the range of achievable topological invariants may become large in Floquet systems, it is important to develop experimental capabilities to reliably detect multiple Floquet topological phases. One promising route is to connect measurements of spin textures in momentum space with various phases with different topological invariants. As a proof-of-principle demonstration, in this paper we first experimentally realize a (periodically modulated) generalized Haldane model (GHM) on a single spin quantum system in diamond and then observe its large-Chern-number Floquet phases by imaging the spin textures.

We choose a driven version of the Haldane Chern insulator model for a number of reasons. First of all, the Haldane model originally describes noninteracting particles hopping in a honeycomb lattice and subject to staggered magnetic flux that breaks the time-reversal symmetry without introducing net magnetic fields [25]. Indeed, the Haldane model serves as a cornerstone in the conceptualization of topological insulators. Second, Floquet driving played a key role in the first realization of the Haldane model using ultracold atoms [15]. However, in cases of high-frequency drivings [26], the experimentally realized Haldane model only exhibits phases with Chern numbers $C = \pm 1$. The high-frequency driving used did not unleash the full power of Floquet driving in realizing topological phases with large topological invariants. Clearly then, to obtain Floquet Chern insulators with large Chern numbers, near-resonant periodic modulation is more suitable because it can reshape the band structure in a nonperturbative manner [5,27–31]. We are thus motivated to start with a realization of the Haldane model using the synthetic dimensions available in a nitrogen-vacancy (NV) system, with its system parameters periodically quenched with time. Note, however, that the focus of this work is on the successful detection of the obtained Floquet topological phases by a scheme adaptable to true condensed-matter systems.

II. THEORY

A Floquet quantum system is described by a Hamiltonian $H(t)$ that is time periodic, i.e., $H(t) = H(t + T)$, with T being the driving period. As we are concerned with the stroboscopic physics of the system, we can focus on its evolution

*These authors contributed equally to this work.
†zhoulw13@u.nus.edu
‡djf@ustc.edu.cn

operator U over a single driving period, which is called the Floquet operator and defined formally as the time-ordered integral $U = \mathcal{T} e^{-(i/\hbar)\int_0^T H(t)dt}$. The eigenvalue equation of U is $U|\psi\rangle = e^{-iE}|\psi\rangle$, which defines the Floquet eigenstate $|\psi\rangle$ and its quasienergy $E \in [-\pi, \pi)$. If $H(t)$ possesses a discrete translational symmetry in space, U will carry the same symmetry and its eigenvalues E could group into bands, which are analog to the energy bands of static periodic systems and are usually dubbed Floquet quasienergy (or Floquet-Bloch) bands. These bands and their Floquet eigenstates could possess topological features that are usually richer than or sometimes go totally beyond the system described by $H(t)$ in its static limit.

Floquet Chern insulators constitute a unique class of nonequilibrium topological matter in Floquet systems. In two dimensions, they are characterized by a set of Floquet quasienergy bands that is gapped from the other bands and possesses a nonvanishing first Chern number. The first Chern number is a topological invariant that can only take quantized integer values. In the case that a single isolated Floquet band is filled, this Chern number can be found by integrating the Berry curvature of Floquet eigenstates in this band over the first Brillouin zone (BZ), a procedure that is similar to how the Chern number is obtained for a static energy band [32]. To be concrete, we now concentrate on a generic two-dimensional two-band lattice model described by the Hamiltonian $H = \sum_{\mathbf{k}\in \mathrm{BZ}} |\mathbf{k}\rangle H(\mathbf{k}) \langle \mathbf{k}|$ in momentum space, with $H(\mathbf{k}) = \mathbf{h}(\mathbf{k}) \cdot \boldsymbol{\sigma} = h_x\sigma_x + h_y\sigma_y + h_z\sigma_z$. Here, $\mathbf{h}(\mathbf{k}) = (h_x, h_y, h_z)$ is a three-component vector, $\boldsymbol{\sigma} = (\sigma_x, \sigma_y, \sigma_z)$ are Pauli matrices, and $\mathbf{k} = (k_1, k_2)$ is the quasimomentum. The Floquet operator of the system describes its evolution over a driving period T (e.g., from $t = 0$ to T), which is given by

$$U = \sum_{\mathbf{k}\in \mathrm{BZ}} |\mathbf{k}\rangle U(\mathbf{k}) \langle \mathbf{k}|, \quad U(\mathbf{k}) = e^{-iT_2\mathbf{h}_2(\mathbf{k})\cdot\boldsymbol{\sigma}} e^{-iT_1\mathbf{h}_1(\mathbf{k})\cdot\boldsymbol{\sigma}}. \quad (1)$$

Here, we set the Planck constant $\hbar = 1$ and utilize a piecewise quench protocol with the period $T = T_1 + T_2$, in which $\mathbf{h} = \mathbf{h}_1$ $(\mathbf{h} = \mathbf{h}_2)$ for $t \in [0, T_1]$ $(t \in [T_1, T])$. The Floquet spectrum of the system is obtained by solving the eigenvalue equation $U(\mathbf{k})|\varphi\rangle = e^{-iE(\mathbf{k})}|\varphi\rangle$, where the quasienergy $E(\mathbf{k}) \in [-\pi, \pi)$. In general, there are two quasienergy bands separated by gaps at $E = 0, \pi$. Performing Taylor expansions for each of the exponential terms in $U(\mathbf{k})$ and recombining the relevant terms, the quasienergy dispersions are found to be $E_\pm(\mathbf{k}) = \pm \arccos[\cos(T_1|\mathbf{h}_1(\mathbf{k})|)\cos(T_2|\mathbf{h}_2(\mathbf{k})|)]$. In the absence of the time-reversal symmetry, each gapped phase of the system could represent a Floquet Chern insulator (FCI) characterized by the Chern number [31]

$$C = \int_{\mathrm{BZ}} \frac{d^2\mathbf{k}}{4\pi} \frac{\mathbf{d}(\mathbf{k}) \cdot [\partial_{k_1}\mathbf{d}(\mathbf{k}) \times \partial_{k_2}\mathbf{d}(\mathbf{k})]}{|\mathbf{d}(\mathbf{k})|^3}. \quad (2)$$

Here, $\mathbf{d}(\mathbf{k}) = (d_x, d_y, d_z)$ is a vector formed by the components of the Floquet effective Hamiltonian $\mathcal{H}(\mathbf{k}) = \mathbf{d}(\mathbf{k}) \cdot \boldsymbol{\sigma} = d_x\sigma_x + d_y\sigma_y + d_z\sigma_z$, with $\mathcal{H}(\mathbf{k}) \equiv \frac{i}{T} \ln U(\mathbf{k})$. In general these components can be obtained from $U(\mathbf{k})$ numerically. When the gap between the two Floquet bands $E_\pm(\mathbf{k})$ closes or reopens at $E = 0$ or $E = \pm\pi$, the system may undergo a topological phase transition followed by the quantized jump of C from one integer to another. Periodic driving fields could further induce many such transitions and yield Floquet bands with large Chern numbers [31].

In experiments, we detect the Floquet Chern number of the system by imaging its spin texture in $\mathbf{k}$ space. Consider a general normalized state $|\psi(\mathbf{k})\rangle = \sum_{s=\pm} c_s(\mathbf{k})|u_s(\mathbf{k})\rangle$ with the quasimomentum $\mathbf{k}$, where $|u_\pm(\mathbf{k})\rangle$ are Floquet eigenstates of $U(\mathbf{k})$ or $\mathcal{H}(\mathbf{k})$ with the quasienergies $E_\pm(\mathbf{k})$. Solving the eigenvalue equation $\mathcal{H}(\mathbf{k})|u_\pm(\mathbf{k})\rangle = E_\pm(\mathbf{k})|u_\pm(\mathbf{k})\rangle$, we can find the explicit form of $|u_\pm(\mathbf{k})\rangle$ as

$$|u_\pm(\mathbf{k})\rangle = \frac{1}{\sqrt{2E_\pm(\mathbf{k})[E_\pm(\mathbf{k}) - d_z]}} \begin{pmatrix} d_x - id_y \\ E_\pm(\mathbf{k}) - d_z \end{pmatrix}. \quad (3)$$

The expectation value of spin σ_j over the state $|\psi(\mathbf{k})\rangle$ is obtained as $\langle\sigma_j\rangle_\mathbf{k} = [|c_+(\mathbf{k})|^2 - |c_-(\mathbf{k})|^2]d_j(\mathbf{k})/E_+(\mathbf{k})$ for $j = x, y, z$. The spin texture is then formed by the configuration of $(\langle\sigma_i\rangle_\mathbf{k}, \langle\sigma_j\rangle_\mathbf{k}, \langle\sigma_l\rangle_\mathbf{k})$ in $\mathbf{k}$ space for any $i, j, l = x, y, z$ with $i \neq j \neq l$. Under the condition $|c_+(\mathbf{k})|^2 \neq |c_-(\mathbf{k})|^2$, the static winding angle (SWA) of the spin texture at each $\mathbf{k}$ is defined as [33]

$$\theta_{jl}(\mathbf{k}) \equiv \arctan\left(\frac{\langle\sigma_j\rangle_\mathbf{k}}{\langle\sigma_l\rangle_\mathbf{k}}\right) = \arctan\left(\frac{d_j}{d_l}\right). \quad (4)$$

Assuming $|c_+(\mathbf{k})|^2 > |c_-(\mathbf{k})|^2$ without loss of generality, we can extract the Chern number C from the spin texture $(\langle\sigma_i\rangle_\mathbf{k}, \langle\sigma_j\rangle_\mathbf{k}, \langle\sigma_l\rangle_\mathbf{k})$ through the relation [33,34]

$$C = \frac{1}{2} \sum_{\mathbf{k}_0\in \mathrm{SPs}} \mathrm{sgn}(\langle\sigma_i\rangle_{\mathbf{k}_0}) w(\mathbf{k}_0), \quad (5)$$

where SPs stands for singularity points. Here, each quasimomentum $\mathbf{k}_0$ resides at a phase singularity of θ_{jl} in $\mathbf{k}$ space, which appears under the condition $\langle\sigma_j\rangle = \langle\sigma_l\rangle = 0$. $w(\mathbf{k}_0)$ is an integer-quantized winding number defined along an infinitesimal clockwise path $S_{\mathbf{k}_0}$ around $\mathbf{k}_0$, i.e.,

$$w(\mathbf{k}_0) = \oint_{S_{\mathbf{k}_0}} \frac{d\mathbf{k}}{2\pi} \partial_\mathbf{k}\theta_{jl}(\mathbf{k}). \quad (6)$$

By preparing the system in the state $|\psi(\mathbf{k})\rangle$ and measuring the spin texture $(\langle\sigma_i\rangle_\mathbf{k}, \langle\sigma_j\rangle_\mathbf{k}, \langle\sigma_l\rangle_\mathbf{k})$ in $\mathbf{k}$ space, the Chern numbers of different FCI phases in the periodically quenched model can be obtained in experiments.

We can also extract the Chern numbers of FCIs from the dynamical spin textures [33,35,36]. To this end, let the state of the system be prepared generally in $|\psi(\mathbf{k})\rangle = \sum_{s=\pm} c_s(\mathbf{k})|u_s(\mathbf{k})\rangle$. After the evolution over ℓ driving periods guided by $U(\mathbf{k})$, it reaches the state $|\psi(\mathbf{k}, \ell T)\rangle = \sum_{s=\pm} c_s(\mathbf{k}) e^{-i\ell E_s(\mathbf{k})}|u_s(\mathbf{k})\rangle$ following the Floquet eigenvalue equation $U(\mathbf{k})|u_s(\mathbf{k})\rangle = e^{-iE_s(\mathbf{k})}|u_s(\mathbf{k})\rangle$ with $s = \pm$, yielding the spin expectation value $\overline{\sigma_j}(\mathbf{k}, \ell T) \equiv \langle\psi(\mathbf{k}, \ell T)|\sigma_j|\psi(\mathbf{k}, \ell T)\rangle$ for $j = x, y, z$. The long-time stroboscopic average of $\overline{\sigma_j}(\mathbf{k}, \ell T)$ is then given by

$$\overline{\sigma_j}_\mathbf{k} = \frac{1}{NT} \sum_{\ell=1}^{N} \overline{\sigma_j}(\mathbf{k}, \ell T) \quad (7)$$

for $N \in \mathbb{Z}$ and $N \gg 1$, from which we obtain the dynamic winding angle

$$\eta_{jl}(\mathbf{k}) = \arctan\left(\frac{\overline{\sigma_j}_\mathbf{k}}{\overline{\sigma_l}_\mathbf{k}}\right). \quad (8)$$

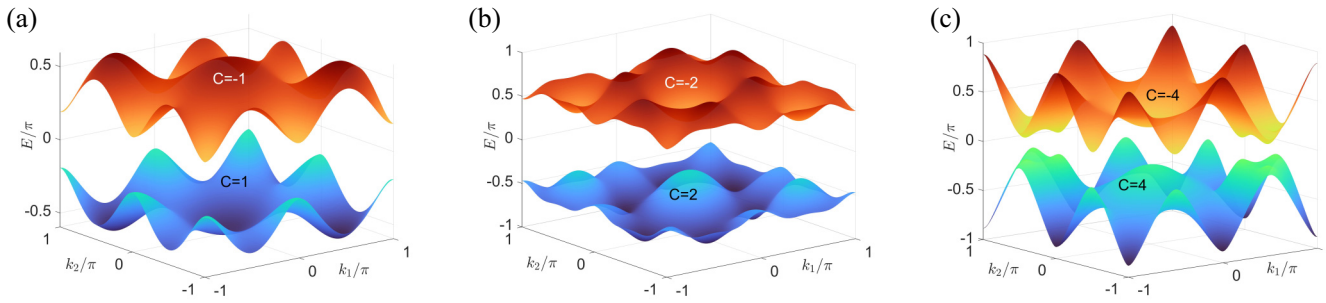

FIG. 1. Quasienergy spectrum of the periodically quenched GHM under periodic boundary conditions. (T_1, T_2) are set as (0.3,0.3), (0.9,0.8), and (0.9,1.2) in (a)–(c), with Chern numbers marked on the two Floquet bands. Other parameters are $(t_1, t_2) = (1, 0.8)$.

In the limit $N \to \infty$ and under the condition $|c_+(\mathbf{k})|^2 > |c_-(\mathbf{k})|^2$, it can be shown that $\eta_{jl}(\mathbf{k}) = \theta_{jl}(\mathbf{k})$ and $\mathrm{sgn}(\langle\sigma_i\rangle_{\mathbf{k}}) = \mathrm{sgn}(\overline{\sigma_i}_{\mathbf{k}})$ [35], with $i, j, l = x, y, z$ and $i \neq j \neq l$. This finally allows us to obtain the Chern number C in Eq. (5) from the long-time averaged dynamic spin texture $(\overline{\sigma_i}_{\mathbf{k}}, \overline{\sigma_j}_{\mathbf{k}}, \overline{\sigma_l}_{\mathbf{k}})$ in $\mathbf{k}$ space. In experiments, the dynamic approach allows one to probe the nonequilibrium Floquet Chern topology without having the complete knowledge about the Floquet Hamiltonian and the initial state.

III. MODEL AND EXPERIMENT

To apply our scheme to the detection of Floquet band Chern numbers in experiments, we start with the Bloch Hamiltonian of a generalized Haldane model and apply time-periodic quenches to its hopping parameters. Expressing the Bloch Hamiltonian of the GHM in the form $H(\mathbf{k}) = \mathbf{h}(\mathbf{k}) \cdot \boldsymbol{\sigma}$, the components in $\mathbf{h}(\mathbf{k}) = (h_x, h_y, h_z)$ are explicitly given by $h_x = t_1(1 + \cos k_1 + \cos k_2) + t_3[2\cos(k_1 - k_2) + \cos(k_1 + k_2)]$, $h_y = t_1(\sin k_1 + \sin k_2) + t_3 \sin(k_1 + k_2)$, and $h_z = 2t_2 \sin\phi[\sin k_1 - \sin k_2 - \sin(k_1 - k_2)]$. Here, t_1, t_2, and t_3 represent the first-, second-, and third-neighbor hopping amplitudes of the GHM. $\phi \in [-\pi, \pi)$ is a phase factor accompanying the second-neighbor hopping. In the static limit, this GHM admits topological phases with a maximal Chern number $C = 2$ [37,38]. Meanwhile, much richer Chern topology could emerge via applying time-periodic quenches to the GHM [31]. In this paper, we realize piecewise periodic quenches of the system parameters (t_3, ϕ), so that $(t_3, \phi) = (0.75, -\pi/6)$ for $t \in [nT, nT + T_1)$ and $(t_3, \phi) = (-0.75, -\pi/2)$ for $t \in [nT + T_1, nT + T_1 + T_2)$. Here, t denotes time, $n \in \mathbb{Z}$, and $T = T_1 + T_2$ represents the driving period. The system Hamiltonians in the time duration T_1 and T_2 have the form of $H(\mathbf{k})$ and differ only in their parameters (t_3, ϕ). Typical spectra of the periodically quenched GHM are shown in Fig. 1, where we observe two Floquet bands $E_\pm(\mathbf{k})$ separated by quasienergy gaps at $E = 0$ and $\pm\pi$. The two bands could touch when $E_\pm(\mathbf{k}) = 0$ or $\pm\pi$, yielding the following gap-closing conditions [31]:

$$\mathbf{h}_1(\mathbf{k})/|\mathbf{h}_1(\mathbf{k})| = \pm\mathbf{h}_2(\mathbf{k})/|\mathbf{h}_2(\mathbf{k})|,$$
$$|\mathbf{h}_1(\mathbf{k})T_1| \pm |\mathbf{h}_2(\mathbf{k})T_2| = n\pi \quad \text{for } n \in \mathbb{Z}. \tag{9}$$

In Fig. 2(a), we report the topological phase diagram of the periodically quenched GHM for different quench durations (T_1, T_2) [31]. Distinct FCI phases carry different Chern numbers C as defined in Eq. (2), and phases with large C $(= \pm4, \pm5, \pm7)$ are observed, which go markedly beyond the allowed Chern insulator phases in the nondriven Haldane model [25,37,38].

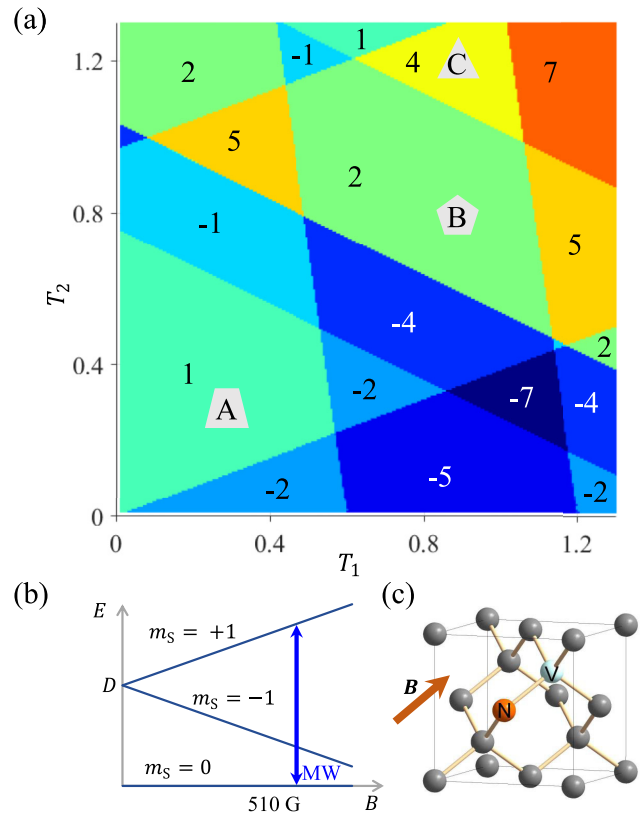

FIG. 2. Topological phase diagram of the periodically quenched GHM and the experimental system. (a) The topological phase diagram in (T_1, T_2) space. Each area of the same color shares the same Chern number as marked therein. The three polygonal markers correspond to the three groups of parameters in our experiments. Other system parameters are $(t_1, t_2) = (1, 0.8)$. (b) Magnetic field dependence of the NV's energy levels in the ground state. A magnetic field of around 510 G parallel to the NV axis is selected in the experiment. MW, microwave. (c) The structure of an NV center in the diamond lattice. The magnetic field is adjusted to be along the NV axis.

We simulate the the periodically quenched GHM by a single spin system and measure its Floquet band Chern number in experiments based on a nitrogen-vacancy (NV) center in diamond [39]. As shown in Fig. 2(c), the NV center [40–42] is a kind of impurity in the diamond crystal lattice. It has emerged as one of the most promising systems for implementing quantum technologies due to its superior optical and spin properties [43,44]. We use the spin state of NV to simulate the Floquet Hamiltonian of GHM in $\mathbf{k}$ space. The NV center is addressed by a home-built confocal microscope. The 532-nm laser which can be switched by an acousto-optic modulator (AOM) is focused into the diamond by an oil objective, and the excited fluorescence can be collected by the same objective and finally detected by an avalanche photodiode with a counter card. In our experiment, an external static magnetic field of around 510 G parallel to the NV symmetry axis [see Fig. 2(b)] is used for polarization of the host ^{14}N nuclear spin, owing to resonant polarization exchanges with the electronic spin in the excited state [45]. The magnetic field is adjusted by a permanent magnet mounted on a three-axis translation stage.

The Hamiltonian of the NV center's electronic ground state with a magnetic field B applied along the NV axis is $H_{\mathrm{NV}} = DS_z^2 + \gamma BS_z$, where S_z is the angular momentum operator for spin 1, $D = 2\pi \times 2870$ MHz is the zero-field splitting, and $\gamma = 2\pi \times 2.8$ MHz/G is the electron's spin gyromagnetic ratio. Here the NV axis is chosen to be the z axis. We can choose an eigenstate $|m_s = +1\rangle$ or $|m_s = -1\rangle$ to form a well-defined qubit with $|m_s = 0\rangle$. The qubit state $|0\rangle$ is selected as $|m_s = 0\rangle$, which is easier to be initialized by laser. Driven by a designed microwave pulse sequence, the Hamiltonian of this subspace, which was employed for the simulation, can then be built using spin-1/2 operators. Here the microwaves driving the evolution of NV spin are generated from an arbitrary waveform generator (AWG), then enhanced by the power amplifier, and finally radiated to the NV center from a coplanar waveguide. All these microwave manipulations and qubit states are described in the rotating frame.

In the SWA experiments shown in Fig. 3, we run the pulse sequence at each pixel in $\mathbf{k}$ space separately. Figure 3(a) shows the pulse sequence used in these experiments. This sequence is composed of three sections: preparation, evolution, and measurement. After going through the preparation section, the qubit state is initialized to $|0\rangle$ by a laser pulse. Then a resonant microwave pulse is applied to drive the state's evolution until the final state becomes an eigenstate of $\mathcal{H}(\mathbf{k})$. To derive the required driving pulse, we take every $\mathbf{k}$ as a control parameter to obtain the Hamiltonian $\mathcal{H}(\mathbf{k})$ and its eigenstates. The shape and duration of the pulse are denoted by $R(\mathbf{k})$ and $\tau(\mathbf{k})$ in Fig. 3(a). The final section is used to measure σ_x, σ_y, or σ_z. For the measurement of σ_x and σ_y, a $\pi/2$ rotation around the direction of $-y$ and x, respectively, is implemented before the optical readout of the NV spin state. This rotation pulse is not needed for σ_z. The final readout of the qubit is obtained by calculating the contrast of the photon count obtained by two counting windows, which correspond to the signal and reference detections. After repeating the sequence 200 000 times and taking the average, we get the value of $\langle\sigma_i\rangle_{\mathbf{k}}$ $(i = x, y, z)$ at each $\mathbf{k}$. Then we figure out the value of the SWA following Eq. (4).

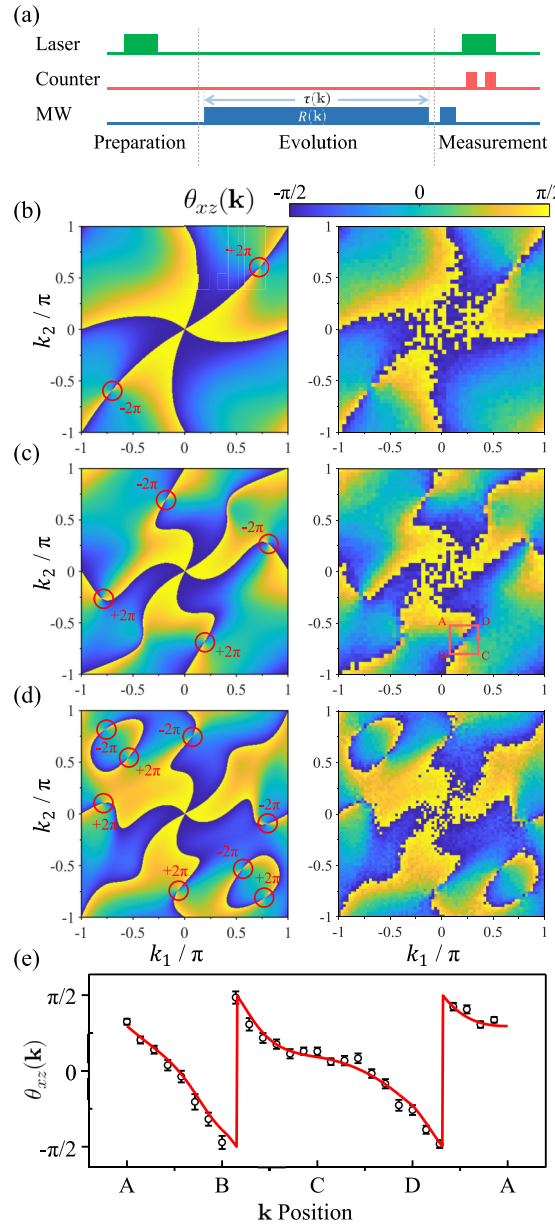

FIG. 3. Static winding angle (SWA). (a) Pulse sequence used for qubit control and measurement in SWA experiments. (b)–(d) show the distributions of SWAs in $\mathbf{k}$ space, with the left and right panels obtained from theory and experiment, respectively. Each singularity point is circled in red and marked with the corresponding winding angle. The parameters in (b), (c), and (d) are set as $(T_1, T_2) = (0.3, 0.3)$, (0.9,0.8), and (0.9,1.2), respectively. Other parameters are the same as those in Fig. 2(a). (e) The SWA distribution on a closed square shown in the right panel in (c). Black circles and the red curve represent experimental and theoretical results, respectively.

In the experiments, we select three representative sets of parameters corresponding to different topological numbers in the phase diagram of the periodically quenched GHM, and detect the distributions of the SWA in $\mathbf{k}$ space, respectively. These selected parameters are marked in Fig. 2(a) and correspond to the three spectra in Fig. 1. Figures 3(b)–(d) show the SWA distributions in $\mathbf{k}$ space obtained

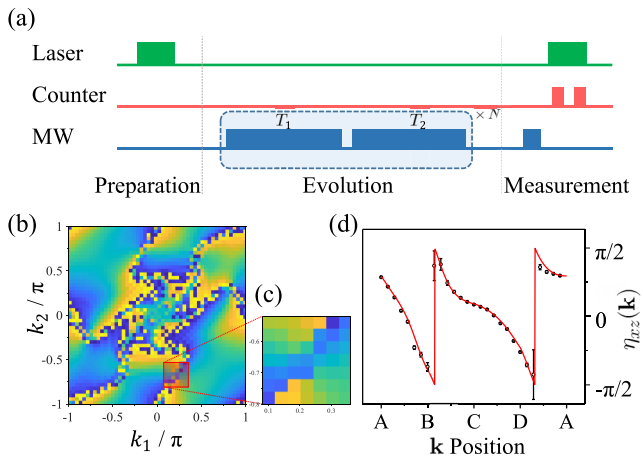

FIG. 4. Dynamical winding angle (DWA). (a) Pulse sequence employed for qubit control and measurement in DWA experiments. (b) The distribution of the DWA in $\mathbf{k}$ space obtained from theoretical calculation. Here the system is evolved over $N = 64$ driving periods under the time-periodic Hamiltonian whose parameters are chosen as $(T_1, T_2) = (0.9, 0.8)$. The rest of the parameters are the same as those chosen for other experiments. (c) Experimental demonstration of the DWA. The value of $\mathbf{k}$ is selected from the marked boxed area in (b). (d) DWA distribution on a closed loop depicted by the square boundary in (c). Black circles represent experimental values, and the red curve shows the theoretical result from the SWA calculations, which are coincident with the DWA in the limit $N \to \infty$. The loop is the same as that used in Fig. 3(c).

theoretically and experimentally. Comparing the left and right panels in Figs. 3(b)–(d), it is clear that our experimental results match the theoretical expectations. The detection of the SWA near each singularity point is crucial to determine the Chern numbers of Floquet bands. In Fig. 3(e), we show the SWA distribution along a closed square marked in Fig. 3(c) to demonstrate the typical singularity with winding number $+1$. Following Eqs. (5) and (6), one can calculate the Chern number using the winding numbers of all singularity points. The weight of each winding number is determined by the sign of $\langle\sigma_i\rangle_{\mathbf{k}}$ which is not used in the calculation of $\theta_{jl}(\mathbf{k})$. The Chern numbers of $\mathcal{H}(\mathbf{k})$ are found to be 1, 2, and 4 in the three groups of experiments.

Beyond the SWA, one can also obtain the Chern number of the system by probing the dynamic winding angle (DWA), which is robust to initial state preparations. We theoretically calculate the distribution of the DWA and show it in Fig. 4(b). The experimental results are shown in Fig. 4(c), and the scanning region of the experiment is the area marked in Fig. 4(b). We show the DWA distribution on the anticlockwise boundary of this area in Fig. 4(d), in order to illustrate the singularity with winding number $+1$. The parameters adopted here are consistent with those in Fig. 3(c), and the state is evolved over $N = 64$ driving periods. The pulse sequence for measuring spin expectation values $\overline{\sigma_j}(\mathbf{k}, \ell T)$ $(j = x, y, z)$ is shown in Fig. 4(a). In the preparation, the spin can be initialized to an arbitrary state. For convenience, the initial state of each experiment is set to $|0\rangle$. During the evolution, the spin state is continually driven for up to $N = 64$ periods, each of which includes two parts that corresponded to parameters $T_1 = 0.9$ and $T_2 = 0.8$, respectively. The measurement section of the experiment is the projection readout of the spin state on the three coordinate axes, which is the same as the last section in Fig. 3(a). Spin expectation values are calculated by averaging all the measurement results after repeating the sequence 200 000 times. After all the data are obtained, we use Eq. (7) to calculate $\overline{\sigma_j}_{\mathbf{k}}$ $(j = x, y, z)$ and get the further calculated $\eta_{jl}(\mathbf{k})$ in Fig. 4(c).

IV. SUMMARY

In this paper, we experimentally realized a periodically quenched generalized Haldane model on an NV center in diamond and observed FCI phases therein with large Chern numbers by imaging the static and dynamic spin textures in the momentum space. Our approach is generic, insensitive to the initial state preparation, and in principle extendable to the realization and detection of FCI phases following arbitrary driving schemes in two-band models. In future work, it would be interesting to consider generalizing our strategy to realize and detect Floquet topological phases in multiband systems, higher spatial dimensions, and other symmetry classes. A particularly interesting class of Floquet matter is the anomalous Floquet topological insulator with winding chiral edge states and unique spatiotemporal topology [12,17,36]. There, the topological invariants are $(2 + 1)$-dimensional winding numbers defined for quasienergy gaps, instead of the Floquet band Chern numbers measured in this paper. An extension of our scheme to realizing and detecting anomalous Floquet phases also forms an intriguing future direction of study.

ACKNOWLEDGMENTS

This work is supported by the National Key R&D Program of China (Grant No. 2018YFA0306600), the National Natural Science Foundation of China (Grants No. 11905211, No. 12275260, No. 81788101, and No. T2125011), the CAS (Grants No. XDC07000000, No. GJJSTD20200001, and No. Y201984), Innovation Program for Quantum Science and Technology (Grants No. 2021ZD0302200 and No. 2021ZD0303204), the Anhui Initiative in Quantum Information Technologies (Grant No. AHY050000), Hefei Comprehensive National Science Center, and the Fundamental Research Funds for the Central Universities.

[1] J. Cayssol, B. Dóra, F. Simon, and R. Moessner, Phys. Status Solidi RRL **7**, 101 (2013).
[2] A. Eckardt, Rev. Mod. Phys. **89**, 011004 (2017).
[3] F. Harper, R. Roy, M. S. Rudner, and S. Sondhi, Annu. Rev. Condens. Matter Phys. **11**, 345 (2020).
[4] M. Rudner and N. Lindner, Nat. Rev. Phys. **2**, 229 (2020).

[5] D. Y. H. Ho and J. Gong, Phys. Rev. Lett. **109**, 010601 (2012).
[6] Q.-J. Tong, J.-H. An, J. Gong, H.-G. Luo, and C. H. Oh, Phys. Rev. B **87**, 201109(R) (2013).
[7] L. Zhou and J. Gong, Phys. Rev. A **97**, 063603 (2018).
[8] A. Agrawal and J. N. Bandyopadhyay, J. Phys.: Condens. Matter **34**, 305401 (2022).
[9] F. Nathan and M. S. Rudner, New J. Phys. **17**, 125014 (2015).
[10] A. C. Potter, T. Morimoto, and A. Vishwanath, Phys. Rev. X **6**, 041001 (2016).
[11] R. Roy and F. Harper, Phys. Rev. B **96**, 155118 (2017).
[12] M. S. Rudner, N. H. Lindner, E. Berg, and M. Levin, Phys. Rev. X **3**, 031005 (2013).
[13] P. Titum, E. Berg, M. S. Rudner, G. Refael, and N. H. Lindner, Phys. Rev. X **6**, 021013 (2016).
[14] L. Zhou and J. Gong, Phys. Rev. B **97**, 245430 (2018).
[15] G. Jotzu, M. Messer, R. Desbuquois, M. Lebrat, T. Uehlinger, D. Greif, and T. Esslinger, Nature (London) **515**, 237 (2014).
[16] L. Asteria, D. T. Tran, T. Ozawa, M. Tarnowski, B. S. Rem, N. Fläschner, K. Sengstock, N. Goldman, and C. Weitenberg, Nat. Phys. **15**, 449 (2019).
[17] K. Wintersperger, C. Braun, F. N. Ünal, A. Eckardt, M. Di Liberto, N. Goldman, I. Bloch, and M. Aidelsburger, Nat. Phys. **16**, 1058 (2020).
[18] T. Kitagawa, M. Broome, A. Fedrizzi, M. S. Rudner, E. Berg, I. Kassal, A. Aspuru-Guzik, E. Demler, and A. G. White, Nat. Commun. **3**, 882 (2012).
[19] M. Rechtsman, J. Zeuner, Y. Plotnik, Y. Lumer, D. Podolsky, F. Dreisow, S. Nolte, M. Segev, and A. Szameit, Nature (London) **496**, 196 (2013).
[20] W. Hu, J. C. Pillay, K. Wu, M. Pasek, P. P. Shum, and Y. D. Chong, Phys. Rev. X **5**, 011012 (2015).
[21] Y. H. Wang, H. Steinberg, P. Jarillo-Herrero, and N. Gedik, Science **342**, 453 (2013).
[22] J. W. McIver, B. Schulte, F.-U. Stein, T. Matsuyama, G. Jotzu, G. Meier, and A. Cavalleri, Nat. Phys. **16**, 38 (2020).
[23] B. Chen, S. Li, X. Hou, F. Ge, F. Zhou, P. Qian, F. Mei, S. Jia, N. Xu, and H. Shen, Photonics Res. **9**, 81 (2021).
[24] T. Oka and S. Kitamura, Annu. Rev. Condens. Matter Phys. **10**, 387 (2019).
[25] F. D. M. Haldane, Phys. Rev. Lett. **61**, 2015 (1988).
[26] T. Oka and H. Aoki, Phys. Rev. B **79**, 081406(R) (2009).
[27] D. Y. H. Ho and J. Gong, Phys. Rev. B **90**, 195419 (2014).
[28] L. Zhou, H. Wang, D. Ho, and J. Gong, Eur. Phys. J. B **87**, 204 (2014).
[29] Z. Zhou, I. I. Satija, and E. Zhao, Phys. Rev. B **90**, 205108 (2014).
[30] H. H. Yap, L. Zhou, J.-S. Wang, and J. Gong, Phys. Rev. B **96**, 165443 (2017).
[31] T.-S. Xiong, J. Gong, and J.-H. An, Phys. Rev. B **93**, 184306 (2016).
[32] D. Xiao, M.-C. Chang, and Q. Niu, Rev. Mod. Phys. **82**, 1959 (2010).
[33] B. Zhu, Y. Ke, H. Zhong, and C. Lee, Phys. Rev. Res. **2**, 023043 (2020).
[34] H. Shen, B. Zhen, and L. Fu, Phys. Rev. Lett. **120**, 146402 (2018).
[35] L. Zhou, Phys. Rev. B **100**, 184314 (2019).
[36] L. Zhang, L. Zhang, and X.-J. Liu, Phys. Rev. Lett. **125**, 183001 (2020).
[37] C. Bena and L. Simon, Phys. Rev. B **83**, 115404 (2011).
[38] D. Sticlet and F. Piéchon, Phys. Rev. B **87**, 115402 (2013).
[39] See Sec. I in the Supplemental Material at http://link.aps.org/supplemental/10.1103/PhysRevB.106.184106 for details about the connection between our model and the manipulation of the NV qubit.
[40] M. W. Doherty, N. B. Manson, P. Delaney, F. Jelezko, J. Wrachtrup, and L. C. L. Hollenberg, Phys. Rep. **528**, 1 (2013).
[41] R. Schirhagl, K. Chang, M. Loretz, and C. L. Degen, Annu. Rev. Phys. Chem. **65**, 83 (2014).
[42] J. Wrachtrup and A. Finkler, J. Magn. Reson. **269**, 225 (2016).
[43] W. Ma, L. Zhou, Q. Zhang, M. Li, C. Cheng, J. Geng, X. Rong, F. Shi, J. Gong, and J. Du, Phys. Rev. Lett. **120**, 120501 (2018).
[44] K. Yang, L. Zhou, W. Ma, X. Kong, P. Wang, X. Qin, X. Rong, Y. Wang, F. Shi, J. Gong, and J. Du, Phys. Rev. B **100**, 085308 (2019).
[45] V. Jacques, P. Neumann, J. Beck, M. Markham, D. Twitchen, J. Meijer, F. Kaiser, G. Balasubramanian, F. Jelezko, and J. Wrachtrup, Phys. Rev. Lett. **102**, 057403 (2009).